NAIC-ID(RS)T-0167-96

NATIONAL AIR INTELLIGENCE CENTER

EXPERIMENTAL INVESTIGATION ON ENERGY DISTRIBUTION OF OUTPUT BEAM OF A POSITIVE-BRANCH CONFOCAL AND UNSTABLE RESONATOR

by

Yan Huizhi

Approved for public release: distribution unlimited

DISCLAIMER NOTICE

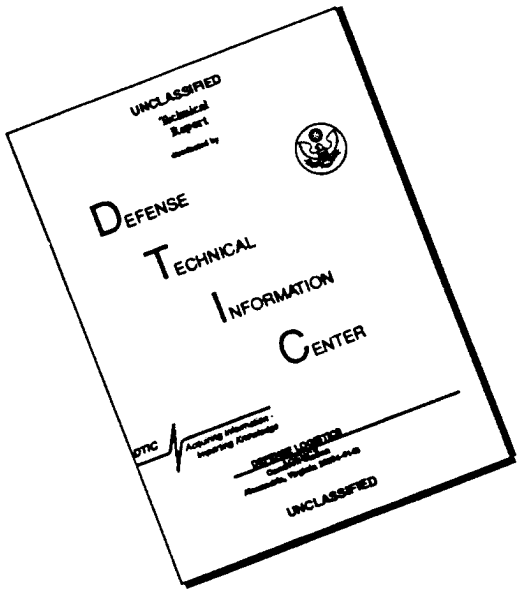

THIS DOCUMENT IS BEST QUALITY AVAILABLE. THE COPY FURNISHED TO DTIC CONTAINED A SIGNIFICANT NUMBER OF PAGES WHICH DO NOT REPRODUCE LEGIBLY.

HUMAN TRANSLATION

NAIC-ID(RS)T-0167-96 26 August 1996

MICROFICHE NR:

EXPERIMENTAL INVESTIGATION ON ENERGY DISTRIBUTION OF OUTPUT BEAM OF A POSITIVE-BRANCH CONFOCAL AND UNSTABLE RESONATOR

By: Yan Huizhi

English pages: 14

Source: Zhongguo Jiguang (Chinese Journal of Lasers), Vol. 16, Nr. 1, 1989; pp. 49-52

Country of origin: China
Translated by: SCITRAN
F33657-84-D-0165
Requester: NAIC/TATD/Bruce Armstrong
Approved for public release: distribution unlimited.

GRAPHICS DISCLAIMER

All figures, graphics, tables, equations, etc. merged into this translation were extracted from the best quality copy available.

EXPERIMENTAL INVESTIGATION ON ENERGY DISTRIBUTION OF OUTPUT BEAM OF A POSITIVE-BRANCH CONFOCAL AND UNSTABLE RESONATOR

Yan Huizhi

ABSTRACT: With regard to combustion driven supersonic diffusion mixed models of continuous wave DF chemical laser positive branch confocal nonstable resonator output beams, experimental research was done on proximate and distant field energy distributions. Measurements clearly showed that test measurements and theoretical analysis were basically in agreement.

KEY WORDS: Supersonic diffusion mixed type chemical laser

I. INTRODUCTION

Due to nonstable resonators being able to attain controlable model volumes and to possess good lateral model discrimination capabilities, as a result, in laser devices where it is necessary to obtain small beam divergence angles and large output powers, extremely wide spread applications have been achieved.

This article reports on research work associated with operating media using supersonic speed flow movements, diffusion mixing, and reaction combustion driven continuous wave deuterium fluoride chemical laser positive-branch confocal nonstable resonator output beam proximate and distant field energy distributions.

II. PRINCIPAL POSITIVE-BRANCH CONFOCAL UNSTABLE RESONATOR PARAMETERS

A positive branch confocal unstable resonator schematic is as shown in Fig.1. It can be completely characterized by the use of two parameters--that is, the round trip geometrical magnification ratio M and the geometrical Fresnel number NO [1].

One gets

$$M = g2/g1 \quad (gi=1-L/Ri) \qquad .$$

In the equation, L is resonator length. Ri is spherical mirror curvature radius.

$$NO = (Ma2)2/L\lambda \qquad .$$

a2 is effective convex reflector radius. λ is laser wave length.

M is an important parameter associated with unstable resonators. A good number of unstable resonator characteristics are intimately related to M. For example, mode selection capabilities and minimum order mode selection capabilities are [1]

$$S = R_{00}/R_{10} = R_{00}/R_{00}^{(2n+l+1)} = M^{-2}/(M^{-2})^2 = M^2$$

In the equations, ROO is the one cycle round trip reflectance in confocal resonators for base modes. R10 is a one cycle round trip reflectance for mode (10).

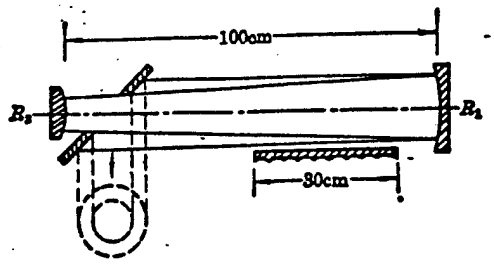

Fig.1 Positive-Branch Confocal Nonstable Resonator

In DF chemical lasers, the influences of flow media nonuniformities on radiation divergences are

$$\theta \approx l\nabla n/(1-1/M) \quad .$$

In the equation, l and ∇n are activation media length and media index of refraction gradients.

In order to avoid the influences of resonator mirror adjustment loss, the vibration tolerance levels allowed in association with concave reflectors are

$$x = \pm(N-1)(\lambda/d)(M-1)/2M \quad .$$

In the equation, N is a predetermined diffraction limit multiple associated with output beam divergence angles. d is proximate field light ring diameter.

Threshold power gains influencing resonator interior extraction efficiencies are

$$g_t = (1/2l) \ln \frac{M^2}{r_1 r_2}$$

r1 and r2 are resonator mirror reflectances. As a result--with regard to a specially designated l--one then has a magnification M associated with threshold value gt produced, which matches requirements. Moreover, relative efficiencies associated with extraction laser powers are in direct proportion to (1-gt/go). go is small signal gain. /50

On the basis of gains inside resonators and factors described above, we select geometrical magnifications M to be 1.5 and 2.6 . Resonator length L = 100cm. When output planar mirror coupling aperture M =1.5, round aperture ϕ = 2.3cm. Square aperture outputs are 0.3cmx2.3cm. When M = 2.6, ϕ = 1.15cm. Round aperture Fresnel numbers are, respectively, 80.5 and 59.2. Dimensions of media areas (that is, spray tube effective length and height) are 30cmx3cm.

III. PROXIMATE FIELD ENERGY DISTRIBUTIONS

Fig.2 is square ring proximate field patterns obtained in association with ouput powers of 3200W and ablated plexiglass at locations 50cm from laser output windows. (a) is a front view. (b) and (c) are side views. Burn loss spot outside ring dimensions are approximately 3.5cmx3.5cm . Inside ring dimensions are 2.3cmx2.3cm. The ratio of inner and outer ring dimensions matching up with the bright rings of proximate fields are equal to resonator round trip magnifications M.

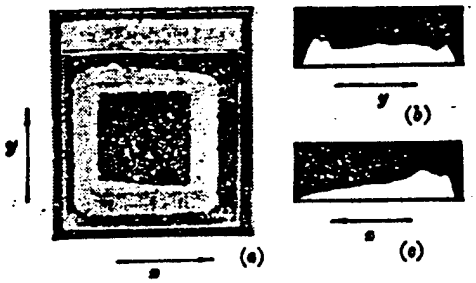

Fig.2 M=1.5 Square Aperture Proximate Field Burn Loss Diagrams

In Fig.2(b), the axis of measurement y is perpendicular to the direction of gas flow and the light axis. Due to the fact that--within a cross section parallel to the plane of the spray nozzle exit--small signal gain distributions are comparatively uniform, as a result, one sees displayed relatively good model characteristics. They are similar to cavity models shown in Fig.3 [2(illegible)].

In Fig.2(c), measurement axis x is parallel to the direction of gas flow, and, in conjunction with this, is perpendicular to the light axis. Due to the influences of activation media, asymmetries are created in gas flow direction light strength distributions. This type of nonuniform gain linearity creates the existence of a peak value in the region of the upper reaches.

When there is an M = 1.5 circular aperture output, output power is 2350W. For the outer ring of plexiglas burn loss diagrams, ϕ = 3.5cm. For inner rings, ϕ = 2.3cm. Side diagrams are similar to square aperture output ablation spots.

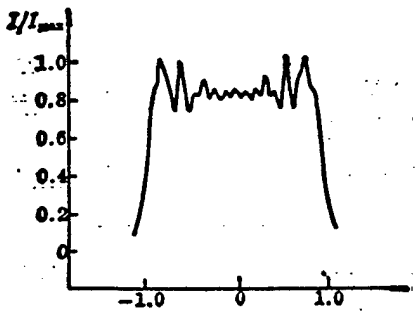

Fig.3 Cavity Proximate Strength Distribution Associated with Output Mirror Surface

IV. DISTANT FIELD ENERGY DISTRIBUTIONS

1. Theoretical Calculations

Due to the geometry of positive-branch confocal nonstable resonators, reproduced wave forms are uniform planar waves. As a result, it is possible to take bright rings uniformly illuminated by planar waves and use them to act as nonstable resonator output beam characteristics. The distant fields are nothing else than a Fulanghefei (phonetic) diffraction pattern. In accordance with diffraction theory, it is posssible to calculate distant field strength angular distributions as [8]:

$$I(\omega)=\frac{I_0}{(1-\varepsilon^2)^2}\left[\frac{2J_1(k d_1\omega)}{k d_1\omega}\right] -\varepsilon^2\left(\frac{2J_1(k\varepsilon d_1\omega)}{k\varepsilon d_1\omega}\right)^2$$

In the equation, ε is the ratio of interior and exterior bright ring diameters in proximate field diagrams, that is

$$\frac{d_2}{d_1}=1/M;$$

J1 is a first order Bessel function. IO is the light strength value associated with the position at the center of distant field patterns. $k = 2\pi/\lambda$. ω is the angular radius in distant field distribution patterns. Let

$$kd1\omega = Z$$

Then,

$$kd_1\omega = Z,$$

$$I(Z) = \frac{I_0}{(1-\varepsilon^2)^2}\left[\frac{2J_1(Z)}{Z}\right] - \varepsilon^2\left(\frac{2J_1(\varepsilon Z)}{\varepsilon Z}\right)^2$$

Distant field relative energy distributions are

$$E^M(Z) = \frac{1}{2(1-\varepsilon^2)^2}\int_0^Z\left[\frac{2J_1(Z)}{Z} - \varepsilon^2\left(\frac{2J_1(\varepsilon Z)}{\varepsilon Z}\right)\right]^2 Z\,dZ$$

With regard to the two forms of operations described above, distant field strength distributions associated with M = 1.5, 2.6, and ∞ as well as energy distribution curves shown in Fig.4 and Fig.5, if one lets distant field full light spot energies be

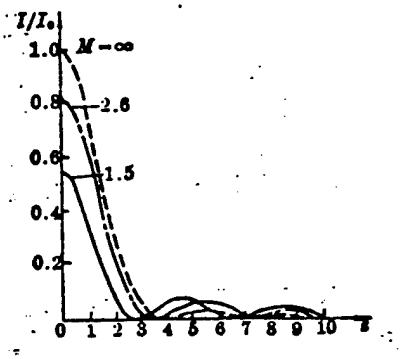

Fig.4 Distant Field Optical Strength Distributions Associated with M = ∞, 2.6, and 1.5

100%, with regard to M = 1.5, the interior of central main lobes account for approximately 30% of total energies. The first side lobes account for 30%. Second side lobes account for 20%. Third side lobes account for 10% ... . As far as M = 2.6 is concerned, central main lobes account for 60.5%. First side lobes account for 28.5% ... . Output beam angles of divergence and focus maculae radii are shown below in accordance with definitions associated with Fig.6 [4].

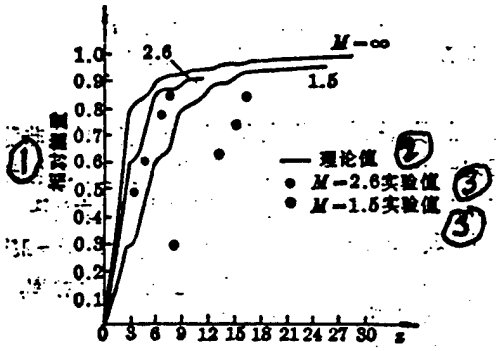

Fig.5 Output Energy Distributions for M = ∞, 1.5, and 2.6

Key: (1) Relative Energy (2) Theoretical Value (3) Experimental Value

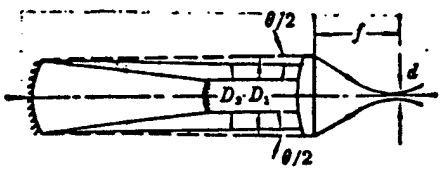

Fig.6 Confocal Nonstable Resonator Beam Divergence and Foci

Divergence angle $\omega = Z(2/\pi)\lambda/d1$. Using 83.8 percent of total energy as the standard, when M = 1.5, Z = 11.8, λ = 3.8x

10-4cm, and d1 = 3.5cm, then, $\omega 1.5$ = 0.815mrad. When M = 2.6, Z = 5.8, λ = 3.8x10-4cm, and d1 = 3cm, then, $\omega 2.6$ = 0.467mrad.

$$f = 111.3\text{cm}, \quad M = 1.5$$

$$D1.5 = f \cdot \omega 1.5 = 0.907\text{mm}.$$

M = 2.6 . Focal maculae diameters are

$$D2.6 = f \cdot \omega 2.6 = 0.519\text{mm}.$$

2. Experimental Research

(1) Ablated Metal Plates Show Distant Field Energy Distributions

As far as light associated with M = 1.5 confocal unstable resonator output beams passing through focusing lenses of f = 111.3cm are concerned, burning losses are placed on black copper metal plates at locations amplified approximately 2.5 times the actual focal point. Ablation power is 1.5kW. Ablation time is 1s. The diffraction pattern photograph is as shown in Fig.7.

From the photograph, it can be seen that the center of the pattern has a diameter of approximately 2mm. With regard to metal surface burn loss striations from being melted, the outsides of melting striations are the original black colored

metal surface which has not yet been changed. The width is very narrow. The most outside ring is a metal surface oxidation layer that has been burned away. The width is approximately ϕinxϕout = 2.3mmx3mm in a red copper colored circular ring.

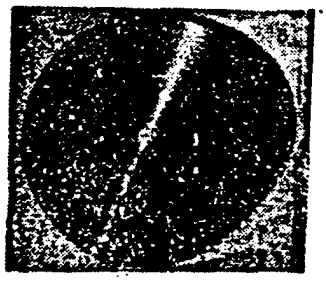

Fig.7 Distant Field Diffraction Pattern Displayed by Ablated Metal Plate M = 1.5, P = 1.5kW (Photograph Magnification 1.5 Time)

Central burn loss melted spot diameter is approximately 2mm. This is due to the distances between main lobes, primary, and secondary side lobes being very close (after magnification of 2.5 times) the first, second, and third dark ring theoretical diameters are, respectively, 0.558mm, 1.270mm, and 1.979mm). The energies which they each account for are relatively large--respectively (illegible)%, 31%, and 20%. Therefore, as far as the patterns displayed for one second burn losses are concerned, it is not possible to separate central lobes from side lobes. The farthest outside ring of red copper colored ablation maculae is caused by third side lobe energies.

Diffraction patterns clearly show that most of the distant field energy envelope associated with M = 1.5 confocal unstable resonators lies within the previous four levels of diffraction ring belts, and theoretical calculation results agree with this.

(2) Distant Field Energy Distributions Associated with Ablated Plexiglass

With regard to confocal unstable resonator output beams with magnifications of M = 1.5 (output power 2.4kW)--because of single lens focusing with focal length of 111.3cm--burn losses are located at a location on the plexiglass magnified 2.5 times the actual focal point. Ablation time is 1s. Fig.8 is a distant field photographic image obtained by ablation. [[1610]]

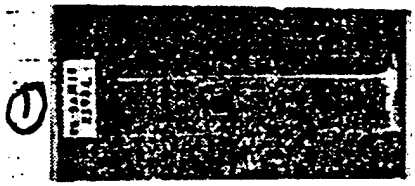

Fig.8 Distant Field Image Obtained for Ablated Plexiglass
M = 1.5, P = 2.4kW
(1) Illegible

Burn loss patterns clearly show that distant field strength distributions are quite uniform and quite symmetrical. Due to the round symmetrical burn loss patterns being rather good, as a result, it is possible to opt for the use of volume calculation methods to calculate angular energy distributions with comparative accuracy. Calculation results are shown in Fig.5. From calculations, one gets the fact that the divergence angle associated with M = 1.5 and 83.8% of total energy contained is 1.09mrad. Focal point diameter is 1.21mm. This is approximately 1.33 times the theoretical value.

In this ablation method, there are the measurement accuracies set out below for influencing factors. a. Due to the fact that plexiglass has a threshold energy density value, it is not then possible to calculate this as lower than for the volumes influenced by the threshold energy density. In particular, when burn losses are relatively shallow, values are comparatively severe. b. Plexiglass lateral thermal conductance, multiple beam reflections on ablation aperture walls, and scattering of light by ablated materials in apertures lead to alterations of corresponding relationships associated with local input energy densities and burn loss depth. Burn losses in lateral directions increase. The influences of this in situations where ablation depths at focal points are very deep are very severe. c. Due to the fact that the focal length of lenses that we opt for the use of is comparatively short and the depth of ablation apertures is

relatively deep (8.8cm)--if the plane of target material initial ends is placed on the focal plane, then, the terminal end of ablation is too far from the focal plane. The distance of deviation from the focal point very, very greatly exceeds focal depth. If the definition of depth of focus is [5] that "the strength of the center of a point light source image does not exceed a certain range of values"--for example, taking the range which is not lower than 80% of the focal point intensity to be the focal depth, then, the depth of focus is

$$|Z_0| < \frac{\lambda}{2}\left(\frac{f}{a}\right)^2$$

In the experiments in question, f = 111.3cm. a = 1.75. λ = 3.8x10-4cm. Substituting in, one obtains $|Z_0| \leq 0.768$ cm. This is a burn loss depth of 1/11.5 . As a result, for target material initial ends placed on focal points, dispersion is then very severe.

In order to eliminate the influences of these three factors, measurements with regard to M = 2.6 opt for the use of infrared scanning methods.

(3) Making Use of One Dimensional Infrared Scanning Methods to Measure Distant Field Distributions /52

Option is made for the use of indium antimonide detectors to measure intensity distributions associated with focal points. Infrared detectors are placed at locations where there is focal point magnification of 2.5 times. As far as ϕ = 0.1mm diaphragms in front of (right next to) detector positions are concerned, samples are used to turn reflected mirror light beams, causing beams to sweep over diaphragms. Powers which beams through diaphragms shine on detectors are directly proportional to distant field intensity distributions. Detector output signals are stored and displayed by transient wave form storage units. Stored signals graph out distribution curves by x-y function recording devices. Experimental systems are as shown in Fig.9.

Fig.10 is distant field intensity distribution curves obtained in association with the use of these methods with regard to confocal unsteady resonator focused beam sweeps. Plexiglas burn loss diagrams under similar conditions clearly show that distant field distributions have comparatively good axial symmetry characteristics. As a result, we believe that sweep images have relatively good axial symmetry characteristics in the same way. From Fig.10, it is possible to see that sweep curve wave valley positions are very close to the locations of dark rings associated with theoretical curves.

Using spherical volume ratio methods in the same way, one obtains relative energy distributions associated with M = 2.6 (Fig.5). In accordance with 83.8% energy calculations, test measurement divergence angles are 0.59mrad. Focal maculae diameters are 0.65mm and are 1.25 times theoretical values.

Calculations clearly show that test measurements in main lobes contain 80.3% of theoretical main lobe energies.

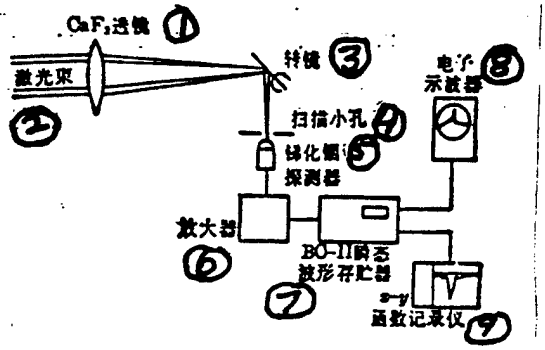

Fig.9 One Dimensional Infrared Scanning Measurement System

Key: (1) Lens (2) Laser Beam (3) Turning Reflector (4) Sweep Aperture (5) Indium Antimonide Detector (6) Magnifier (7) BC-II Transient Wave Form Storage Unit (8) Electronic Display (9) x-y Function Recorder

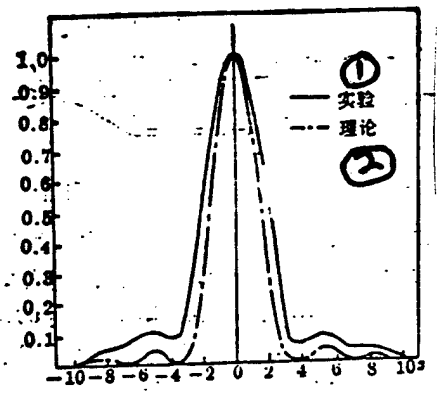

Fig.10 Distant Field Intensity Distribution Curves (1) Actual Value (2) Theory

REFERENCES

1 Chester A. N., *Appl. Opt.*, 11(11), 2584(1972)

2 Gross R. W., Bott J. F., "Handbook of Chemical Lasers"(John Wiley & Sons, New York, 1976), p. 132

3 Born M. and Wolf E., "Principles of Optics" (Sixth Edition, Pergamon Press, 1980), p. 416

4 永久治彦ほか, 光学, 14(3), 185～190 (1985)

5 久保田广, 刘瑞祥译"波动光学"(科学出版社, 1983), pp. 393～394